

TREBALL FINAL DEL GRAU EN ENGINYERIA FÍSICA

# The evolution of tidal streams in the aftermath of white dwarf mergers

FERNANDO MARTÍNEZ MURILLO  
PABLO LORÉN AGUILAR  
ENRIQUE GARCÍA-BERRO MONTILLA  
UNIVERSITY OF EXETER, UNITED KINGDOM  
JUNE, 2017

# ABSTRACT

In this work, a series of Smoothed Particle Hydrodynamics simulations of the coalescence between two He and CO white dwarfs is presented. The simulations discussed here encompass a wide range of stellar masses that are representative of the Galactic white dwarf field population. Both the chemical and the hydrodynamical evolution of the mergers simulated here have been analyzed in detail. This has allowed us to characterize possible different outcomes for the merger and to calculate its potential observational signatures, such as the associated gravitational waveforms, the expected number of neutrinos emitted, the fallback luminosities, and the emitted light curves. Special attention has been paid to the formation and evolution of the tidal stream formed during the process of disruption of the secondary white dwarf. Unlike any previous study in the subject, we have been found that the tidal stream is fragmented. Its potential consequences have been explored and possible different explanations for this have been considered.

**Keywords:** white dwarfs, binaries, mergers, supernovae, smoothed particle hydrodynamics, tidal streams, gravitational waves, light curves, neutrinos, X-ray luminosities, optical luminosities.



# CONTENTS

<b>1. INTRODUCTION</b>	<b>1</b>
<b>2. WHITE DWARFS</b>	<b>4</b>
2.1. Binary white dwarf mergers	5
<b>3. NUMERICAL METHODS</b>	<b>7</b>
3.1. Initial white dwarf models	9
3.2. Observational signatures	11
<b>4. RESULTS</b>	<b>16</b>
4.1. Time evolution of the merging process	16
4.2. Definition of the radii of the merger remnant	18
4.3. Characteristics of the merger remnant	19
4.4. Evolution of the tidal stream	22
4.5. Abundance profiles	23
4.6. Observational signatures of the mergers	26
<b>5. SUMMARY AND CONCLUSIONS</b>	<b>32</b>
<b>6. REFERENCES</b>	<b>34</b>



# 1. INTRODUCTION

Thermonuclear supernovae, also known as Type Ia Supernovae (SN Ia), originate from the explosion of carbon-oxygen white dwarfs [Hillebrandt et al. [2013](#); Ruiz-Lapuente [2014](#)]. These explosions are one of the most energetic events in the Universe. Additionally SN Ia are one of the best distance indicators, since they can be seen at very large distances. Moreover, the homogeneity of their observed light curves allows us to use them as standard candles. However, the nature of the progenitor systems of SN Ia remains still uncertain and it is a topic of active research. There are six possible scenarios that try to explain how the system evolves to a thermonuclear detonation. All of them have advantages and drawbacks [Tsebrenko & Soker [2015](#)]. In fact, all of them could contribute to the total SN Ia rate. We list these scenarios in alphabetical order:

- a) The core-degenerate scenario (CD) [Livio & Riess [2003](#); Kashi & Soker [2011](#); Soker [2011](#); Ilkov & Soker [2012](#), [2013](#); Soker et al. [2013](#); Aznar-Siguán et al. [2015](#)]: During common envelope evolution, a white dwarf merges with the hot core of a massive asymptotic giant branch (AGB) star. The detonation might occur before expelling the entire common envelope or long time after the merger.
- b) The double-degenerate scenario (DD) [Webbink [1984](#); Iben et al. [1984](#)]: The detonation occurs after two white dwarfs merge, but it is not clear how long after the merger the explosion of the remnant takes place [van Kerkwijk et al. [2010](#)]. [Tornambé & Piersanti [2013](#)] consider very long delays from merger to explosion.
- c) The double-detonation mechanism (DDet) [Woosley & Weaver [1994](#); Livne & Arnett [1995](#); Shen et al. [2013](#)]: A sub-Chandrasekhar mass WD accumulates a layer of helium-rich material on its surface. This layer is compressed as more material is accreted and detonates, leading to a second detonation near the center of the primary white dwarf.
- d) The single degenerate scenario (SD) [Whelan & Iben Jr. [1973](#); Nomoto [1982](#); Han & Podsiadlowski [2004](#)]: A non-degenerate stellar companion transfer mass to a white dwarf and then it explodes when the Chandrasekhar mass limit is reached.
- e) The white dwarf-white dwarf collision scenario (WWC) [Raskin et al. [2009](#); Rosswog et al. [2009](#); Lorén-Aguilar et al. [2010](#); Thompson [2011](#); Kushnir et al. [2013](#); Aznar-Siguán et al.

- f) [2013](#), [2014](#)]: Two white dwarfs collide and immediately ignite the nuclear reaction that powers the detonation.
- g) The singly-evolved star scenario (SES) [Chiosi et al. [2015](#)]: Pycnonuclear reactions drive powerful detonations in single carbon-oxygen white dwarf. This scenario is relatively undeveloped

The coalescence of two white dwarfs (the so-called DD scenario) is thought to be one of the most common destinies of the evolution of binary systems, since white dwarfs are the most common endpoint of stellar evolution. The merger of two white dwarfs has been studied extensively in the past. For instance, the pioneering work of [Mochkovitch & Livio [1989](#); [1990](#)], who used an approximate method (the so-called Self-Consistent-Field method, [Clement [1974](#)]). Later, [Benz et al. [1989a](#), [1989b](#), [1990](#); Rasio & Shapiro [1995](#); Segretain et al. [1997](#)] studied the problem using reduced resolutions and the classical expression for the artificial viscosity [Monaghan & Gingold [1983](#)]. To overcome these shortcomings the simulations of [Guerrero et al. [2004](#)] opened the way to more realistic simulations, using an increased number of SPH particles and an improved prescription for the artificial viscosity. More recently, the simulations of [Yoon et al. [2007](#); Lorén-Aguilar et al. [2005](#), [2009](#)] were carried out using modern prescriptions for the artificial viscosity and even larger numbers of particles.

All the previous simulations show that during the merger the secondary star is totally disrupted. The mass transfer process from the secondary white dwarf to the primary star forms a hot corona around the more massive white dwarf and a Keplerian disk around it. If the central object reaches the Chandrasekhar mass limit, a SN Ia occurs. However, there are some cases where a SN Ia can be produced without reaching the Chandrasekhar mass limit. In fact, this scenario will be studied in this project. This hypothesis has been also studied previously. For instance, previous works about this issue are those of [Bildsten et al. [2007](#); Shen & Bildsten [2009](#), [2014](#)]. Finally, we mention that [Papish et al. [2015](#)] performed a series of 2D simulations to study the response of a donor He white dwarf to an exploding carbon-oxygen white dwarf of around 1.0-1.1 solar masses, which is below the Chandrasekhar limit.

This project is organized as follows. First, in Sect. 2, we provide some theoretical background about white dwarfs and the merger process. Sect. 3 is devoted to explain the main features of the code used and the methods employed to characterize the observational signatures of the merger. It follows Sect. 4, where the results of the simulations are presented and analyzed in detail. Specifically, in Sect. 4.1 the time evolution of the merger and its remnant is studied. Then, in Sect. 4.2 the definition of the outer edges of each of the region of the merger remnant are provided. In Sect. 4.3, the characteristics of the merger

remnant are shown. The tidal stream features are studied such as its formation and fragmentation in sect. 4.4, while in Sect. 4.5 the time evolution abundance profile of the coalescence is discussed. Finally, in Sect. 4.6 the results of the possible observational signatures are analyzed. To sum up, in Sect. 5 a summary of the most relevant results are discussed.

## 2. WHITE DWARFS

White dwarfs are the final evolutionary state of all stars that do not have enough mass to form a neutron star or a black hole, or to explode as a supernova. Their mass is comparable to that of the Sun, while its volume is comparable to that of the Earth, which means they have very high densities. White dwarfs will be the final evolutionary state of 95% of the stars currently on the main sequence.

High-density regions of the interstellar medium form clouds made of gas (mainly hydrogen and helium) and dust. Under certain circumstances, such clouds collapse, leading to formation of regions with enough temperature and density to ignite hydrogen and form stars. During the so-called main sequence phase, stars remain in hydrostatic equilibrium, burning hydrogen steadily, and temperature is the key control parameter to stabilize the star. During this stage, the luminosity of the star depends on its mass.

After consuming most of its hydrogen, stars will follow different evolutionary paths depending on their mass. Fig. 1 illustrates the different evolutionary stages of stars in the Hertzsprung-Russell diagram. If the mass of the star is smaller than a few solar masses, the main sequence star will expand, becoming a red giant. Subsequently, the outer layers of the red giant will be ejected and the remnant will become a white dwarf. If the mass of the star is larger than about 11-12 solar masses, the core of the star will collapse and form a Type II supernova, leaving as remnant either a neutron star or a black hole.

Isolated white dwarfs do not have large enough temperatures to burn thermonuclear fuels. Consequently, the only way to balance the mechanical structures of these stars (namely, their self-gravity) is the gradient of pressures of degenerate electrons, which does not depend on the temperature. It can be proven that this results in a very specific relation between the radius and the mass of the white dwarf at moderately high temperatures,  $R \sim M^{-1/3}$ . Also, it can be proven as well that at high densities electrons become relativistic resulting in the existence of a maximum limiting mass that degenerate electrons can support. This limit is known as the Chandrasekhar limiting mass, and its value is about 1.45 solar masses.

Finally, the chemical composition of white dwarfs depends on their mass. White dwarfs with masses lower than 0.45 solar masses are made of pure helium. If its mass is within the interval ranging from 0.45 to 1.1 solar masses, the chemical composition is roughly 40% carbon and 60% oxygen, although they are not uniformly distributed throughout the star. Finally, white dwarfs more massive than 1.1 solar masses are made of a mixture of oxygen and neon [Ritossa et al. [1996](#)]

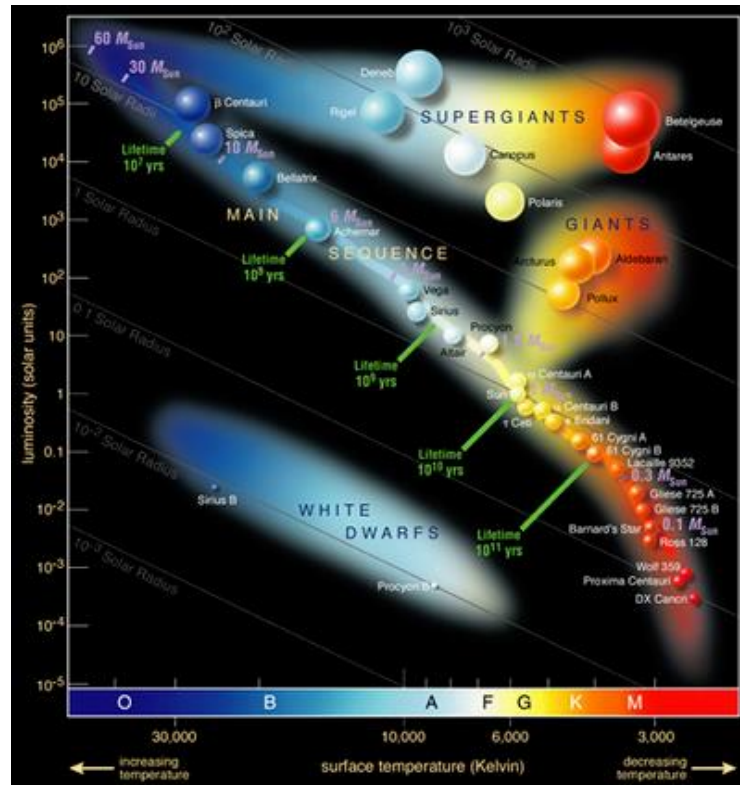
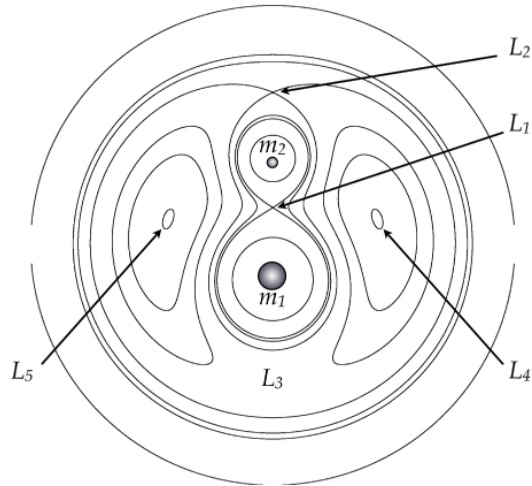


Figure 1. Hertzsprung-Russell diagram

## 2.1. Binary white dwarf mergers

Roche lobes are the regions around a star in a binary system where the material that lies inside remains gravitationally bound to the star. It can also be more technically defined as the zero-level curve of the energy potential of each star. Close to each star, the gravitational equipotential surfaces are approximately spherical and concentric. On the contrary, far from the stars, the gravitational influence of the companion plays a relevant role, and the equipotential surfaces are deformed. The point where the lobes for each star intersect is known as the Lagrangian point L1 (see Fig. 2), and the corresponding equipotential surface as the Roche lobe. When some material of the less massive star overflows the Roche lobe, it will be transferred to the more massive star through this point. In a binary system with a synchronous rotation circular orbit, there are five Lagrangian points, which co-rotate with the system.



**Figure 2.** Equipotential lines in a binary system as well as the different Lagrangian points.

When the less massive white dwarf overflows the Roche lobe, mass transfer starts. During this episode, the donor star rapidly synchronizes, whereas the more massive one does not. Consequently, orbital angular momentum is transferred from the orbit to the less massive star, thus reducing the orbital separation. This, in turn, increases the mass transfer rate and the final result is that the secondary white dwarf is disrupted and accreted to the more massive star when its potential energy becomes positive. However, we note that mass transfer can be stable, depending on the mass star ratio [Lorén-Aguilar et al. 2009]. After the secondary has been totally disrupted most of the material is accreted by the primary white dwarf and little mass is ejected from the system (about  $10^{-3}$  solar masses). The configuration of the remnant is the following. First the primary remains almost unchanged, the only difference is that it has been spun up, and rotates as rigid body. On top of it is found a region formed by the material accreted during the first phases of the merger. This material has been compressed and heated. Consequently this region is hot, and a convective shell is formed. Moreover, this region rotates rapidly, owing to angular momentum conservation. Finally, surrounding this region a debris region contains most of the material of the secondary that has not been accreted.

# 3. NUMERICAL METHODS

The hydrodynamical evolution of the white dwarf binary system is followed using the Smoothed Particle Hydrodynamics (SPH) numerical technique [Lucy [1977](#); Gingold & Monaghan [1977](#)]. Since it is a purely Lagrangian method, it does not require a grid, making it ideally suited for the study of three-dimensional phenomena with arbitrary geometries. The SPH code used for this project is specifically adapted for the study of stellar binary mergers, and has been used in several similar studies in the past [Guerrero et al. [2004](#); Yoon et al. [2007](#); Lorén-Aguilar et al. [2005](#), [2009](#)].

The hydrodynamical equations solved in the SPH code are:

$$\frac{d\mathbf{v}}{dt} = -\nabla \frac{P}{\rho} + \mathbf{f} \quad (1)$$

$$\frac{du}{dt} = -Pd \left( \frac{V}{m} \right) = \frac{P}{\rho^2} \frac{d\rho}{dt} = -\frac{P}{\rho} \nabla \cdot \mathbf{v} \quad (2)$$

$$TdS = C_v dT + T \left( \frac{\partial P}{\partial T} \right)_v dV \quad (3)$$

These equations are, respectively, Euler's equation, the first law of thermodynamics, and the first  $TdS$  equation. Using a smoothing function (usually known as kernel), these equations can be discretized in a set of volume elements, which we will call particles. The smoothed approximation of an arbitrary function  $f(\mathbf{r})$  is

$$\tilde{f}(\mathbf{r}) = \sum_i \frac{m_i}{\rho_i} f(\mathbf{r}_i) W(\mathbf{r} - \mathbf{r}_i, h) \text{ with } \lim_{h \rightarrow 0} \int W(\mathbf{r} - \mathbf{r}', h) d^3\mathbf{r}' = 1 \quad (4)$$

where  $W$  is the smoothing kernel. The kernel only depends on the distance between particles and  $h$ , the smoothing length, which can be interpreted as the typical radius of each SPH particle. The kernel used in this work is the standard polynomic kernel of [Monaghan & Lattanzio [1985](#)]. The gravitational forces are evaluated using an octree [Barnes & Hut [1986](#)] in order to reduce the computational cost. In order to keep numerical stability in the presence of shocks, the code uses a prescription for the artificial viscosity based in Riemann-solvers [Monaghan [1997](#)]. Moreover, to suppress artificial viscosity in pure shear flows, the viscosity switch of [Balsara [1995](#)] is also used. In this way, the dissipative terms are only present whenever necessary, reducing as much as possible any undesirable excess of numerical dissipation.

Using the aforementioned approximations, Eqs. (1-3) can be rewritten as

$$\frac{d\mathbf{v}_i}{dt} = - \sum_j m_j \left( \frac{P_i}{\rho_i^2} + \frac{P_j}{\rho_j^2} - \alpha \frac{v_{ij}^{sig}}{\bar{\rho}_{ij}} \mathbf{v}_{ij} \cdot \hat{\mathbf{e}}_{ij} \right) \mathbf{r}_{ij} F_{ij} \quad (5)$$

$$\frac{du_i}{dt} = \frac{P_i}{\rho_i^2} \sum_j m_j \mathbf{v}_{ij} \mathbf{r}_{ij} \bar{F}_{ij} - \frac{1}{2} \sum_j m_j \alpha \frac{v_{ij}^{sig}}{\bar{\rho}_{ij}} (\mathbf{v}_{ij} \cdot \hat{\mathbf{e}}_{ij})^2 |\mathbf{r}_{ij}| \bar{F}_{ij} \quad (6)$$

$$\frac{dT_i}{dt} = - \sum_j \frac{m_j}{(C_v)_j} \frac{T_j}{\rho_i \rho_j} \left[ \left( \frac{\partial P}{\partial T} \right)_\rho \right]_j \mathbf{v}_{ij} \cdot \nabla_i W(|\mathbf{r}_{ij}|, h) + q_{\text{visc}} \quad (7)$$

where  $\bar{\rho}_{ij} = (\rho_i + \rho_j)/2$  and  $\bar{F}_{ij} = (F_i + F_j)/2$ , and  $F$  is a positive definite function that only depends on  $|\mathbf{r}_{ij}|$  and on the smoothing kernel  $h$ , used to express gradient of the kernel  $\nabla W_{ij} = \bar{F}_{ij} \mathbf{r}_{ij}$ . The signal velocity is taken as

$$v_{ij}^{sig} = c_i + c_j - 4\mathbf{v}_{ij} \cdot \hat{\mathbf{e}}_{ij}, \quad \alpha = 0.5$$

and  $q_{\text{visc}}$  is the viscous dissipation, which is the second term of Eq. (6). The rest of the symbols have their usual meaning.

It is worth noting that the code evolves the thermal energy in two ways. In most instances, Eq. (6) is used in the code, since it guarantees exact energy conservation. However, in regions where the degeneracy is high, a small change in thermal energy can lead to a huge change in temperature, introducing numerical noise. If such jump in temperature is detected, the variation of thermal energy in the gas is computed using Eq. (7). Evolving the thermal energy through its temperature does not guarantee energy conservation anymore in the SPH scheme, but it turns out to be more stable numerically. Since the number of times this alternative method has to be used is relatively small, overall energy conservation remains under acceptable levels ( $\sim 1\%$ ), and the numerical stability of the scheme is granted.

The equation of state adopted for the white dwarf is the sum of three different components. Firstly, ions are treated as an ideal gas, but taking into account the Coulomb corrections [Segretain et al. [1994](#)]. Secondly, the pressure of photons is also incorporated. It is a dominant source of pressure in regions with high temperatures and low densities (when nuclear reactions became relevant). Finally, the most important contribution is the pressure of degenerate electrons, which is computed integrating the Fermi-Dirac integrals.

Another important feature of the code is the nuclear network [Benz et al. [1989a](#)]. The code incorporates 14 nuclei: He, C, O, Ne, Mg, Si, S, Ar, Ca, Ti, Cr, Fe, Ni and Zn, and the considered reactions are: the captures of  $\alpha$  particles and its associated back reaction, rates of two C nuclei and the reaction between C and O nuclei. All the reaction rates

are taken from [Rauscher & Thielemann 2000] and the screening factors adopted here are those of [Itoh et al. 1979]. The nuclear energy release is computed independently of the dynamical evolution, using much shorter time steps, and assuming that the dynamical variables of the gas do not change much during these time steps. Moreover, neutrino losses have also been included according to the formulation of [Itoh et al. 1996] for the pair, photo, plasma, and bremsstrahlung neutrino processes.

Regarding the integration method, a predictor-corrector numerical scheme is used with variable time steps [Serna 1996]. Starting from the known values of positions and velocities at time  $t$ , the hydrodynamical equations Eqs. (5-7) are calculated and integrated using a first-order method. These values of position, velocity, internal energy and temperature are the predicted ones at  $t+\Delta t$  and denoted as  $\mathbf{r}', \mathbf{v}', u'$  and  $T'$ . The corrected quantities are

$$\mathbf{r}(t + \Delta t) = \mathbf{r}'(t + \Delta t) + \frac{1}{6}(\mathbf{a}'(t + \Delta t) - \mathbf{a}(t))\Delta t^2 \quad (8)$$

$$\mathbf{v}(t + \Delta t) = \mathbf{v}'(t + \Delta t) + \frac{1}{2}(\mathbf{a}'(t + \Delta t) - \mathbf{a}(t))\Delta t \quad (9)$$

$$u(t + \Delta t) = u'(t + \Delta t) + \frac{1}{2}(\dot{u}'(t + \Delta t) - \dot{u}(t))\Delta t \quad (10)$$

$$T(t + \Delta t) = T'(t + \Delta t) + \frac{1}{2}(\dot{T}'(t + \Delta t) - \dot{T}(t))\Delta t \quad (11)$$

### 3.1. Initial white dwarf models

In order to set up the initial conditions for a simulation, an initial model of white dwarf must be constructed by solving the Lane-Emden equation. The radius of a white dwarf for a given mass can be found integrating the equation of continuity,

$$\frac{dm}{dr} = 4\pi r^2 \rho \quad (12)$$

and the equation of hydrodynamic equilibrium

$$\frac{1}{\rho} \frac{dP}{dr} = -\frac{Gm}{r^2} \quad (13)$$

A polytropic approximation is used,

$$P = K\rho^\gamma = K\rho^{(n+1)/n} \quad (14)$$

where  $P$  is the gas pressure,  $K$  is a constant,  $\rho$  is the density,  $\gamma$  the adiabatic index and  $n$  is the polytropic index. For white dwarfs, the adiabatic index  $\gamma$  is equal to 5/3 and the polytropic index, 3/2. Applying the following change of variable,

$$r = \alpha\xi \text{ and } \rho(r) = \rho_c\theta^n(\xi) \quad (15)$$

where  $\rho_c$  is the central density, the Lane-Emden equation is obtained:

$$\frac{1}{\xi^2} \frac{d}{d\xi} \left( \xi^2 \frac{d\theta}{d\xi} \right) = -\theta^n \quad (16)$$

The boundary conditions are  $\theta(0) = 1$ , because at the center of the star the density is the central one and

$$\left( \frac{d\theta}{d\xi} \right)_{\xi=0} = 0,$$

since the pressure gradient in the center has to be zero. Note that the solution only depends on the polytropic index  $n$ , so it can be solved independently of the value of the mass, meaning that the solution is the same for each simulation. Once the solution is found, the radius of the white dwarfs is found using Eq. (15):

$$R = \alpha\xi_1 = \sqrt{\frac{n+1}{4\pi G} K \rho_c^{(1/n-1)}} \xi_1 \quad (17)$$

where  $\xi_1$  is the first zero of the solution  $\theta(\xi)$ , which is 3.65375 for this  $n$ . The value of  $\rho_c$  can be computed using the value of the mass and integrating Eq. (12)

$$M = \int_0^R 4\pi r^2 \rho dr = 4\pi \left( \frac{(n+1)K}{4\pi G} \right)^{3/2} \rho_c^{(3-n)/2n} \xi_1^2 \left( \frac{d\theta}{d\xi} \right)_{\xi=\xi_1} \quad (18)$$

Then, a set of equal mass particles is distributed at random positions inside a sphere of this radius. In order to relax the initial model, the code is run keeping constant the temperature constant ( $10^7$ K). The simulation is stopped when potential, kinetic, and thermal energy of the system reach a steady state. The process is repeated to generate all the white dwarf models with different masses.

As already explained in Sect. 2, the chemical composition of white dwarfs depends on its mass. White dwarfs with masses smaller than 0.45 solar masses are made of pure helium. If the mass lies between 0.45 and 1.1 solar masses, the chemical composition is 40% of carbon and 60% of oxygen that we assume are uniformly distributed throughout the star.

Once all initial star models are generated and relaxed, binary initial models can be computed. In order to set up the simulation, two relaxed white dwarf models are put at a given distance. Each star is then given the necessary amount of angular velocity to set them in a circular orbit around the center of mass of the system. The binary initial model is setup, and the simulation can be started. During the beginning of the coalescence and until the secondary star fills its Roche lobe, a small acceleration term is added to artificially decrease the separation between both white dwarfs. From this moment on, this acceleration is suppressed, and the system self-consistently evolves until the merger of both stars occurs.

In this work, five different simulations were made. The masses of the binary systems were 0.2+0.6, 0.3+0.6, 0.4+0.6 and 0.3+1.0 solar masses respectively. In four of the simulations, 200k particles were used for each star. In addition, to check the impact of resolution on the final results, one of the runs, the binary system made of 0.3+0.6 white dwarfs, was simulated with an increased number of particles (500k particles for the secondary and 100k particles for the primary), henceforth distinguished from the other by HR.

## 3.2. Observational signatures

In what follows, we proceed to explain how the different potential observational signatures of a white dwarf merger were computed. This includes: emission of gravitational waves, thermal neutrino events, and fallback X-ray luminosity of the remnants.

### 3.2.1. Gravitational waves

Gravitational waves were computed using the slow-motion, weak-field quadrupole approximation [Misner et al. 1973]. Specifically, the procedure outlined in [Lorén-Aguilar et al. 2005] was closely followed. The strain amplitudes can be expressed as:

$$h_{jk}^{TT}(t, \mathbf{x}) = \frac{G}{c^4 d} (A_+(t, \mathbf{x}) \mathbf{e}_{+jk} + A_x(t, \mathbf{x}) \mathbf{e}_{xjk}) \quad (19)$$

where  $d$  is the distance to the source and the polarization tensor coordinate matrices are defined as

$$\mathbf{e}_{+jk} = \frac{1}{\sqrt{2}} [(\mathbf{e}_x)_j (\mathbf{e}_x)_k - (\mathbf{e}_y)_j (\mathbf{e}_y)_k] \quad (20)$$

$$\mathbf{e}_{xjk} = \frac{1}{\sqrt{2}} [(\mathbf{e}_x)_j (\mathbf{e}_y)_k - (\mathbf{e}_y)_j (\mathbf{e}_x)_k] \quad (21)$$

and

$$A_+(t, \mathbf{x}) = \ddot{Q}_{xx} - \ddot{Q}_{yy}, \quad A_x(t, \mathbf{x}) = 2\ddot{Q}_{xy} \quad (22)$$

for  $i = 0$ , and

$$A_+(t, \mathbf{x}) = \ddot{Q}_{zz} - \ddot{Q}_{yy}, \quad A_x(t, \mathbf{x}) = -2\ddot{Q}_{yz} \quad (23)$$

for  $i = \pi/2$ , being  $i$  the angle with respect to the line of sight. In these expressions  $Q$  is the quadrupole moment of the mass distribution. Since the simulations are made of particles, the second time derivative of  $Q$  is expressed in the following way:

$$\ddot{Q}_{jk}^{TT} \approx P_{ijkl}(\mathbf{N}) \sum_p m_p [2\mathbf{v}_p^k \mathbf{v}_p^l + \mathbf{x}_p^k \mathbf{a}_p^l + \mathbf{x}_p^l \mathbf{a}_p^k] \quad (24)$$

where  $m_p, \mathbf{x}_p, \mathbf{v}_p$  and  $\mathbf{a}_p$  are, respectively, the mass, the position, the velocity and the acceleration of each particle and

$$P_{ijkl}(\mathbf{N}) \equiv (\delta_{ik} - N_i N_k)(\delta_{jl} - N_j N_l) - \frac{1}{2}(\delta_{ij} - N_i N_j)(\delta_{kl} - N_k N_l) \quad (25)$$

is the transverse-traceless projection operator onto the plane orthogonal to the outgoing wave direction,  $\mathbf{N}$ . Once the gravitational waveforms are computed for both polarizations, the Fourier transformation of each signal is calculated

$$\tilde{h}(f) = \int_{-\infty}^{\infty} e^{2\pi i f t} h(t) dt \quad (26)$$

as well as the dimensionless Fourier transform

$$H = \frac{\tilde{h}(f)}{T} \quad (27)$$

being  $T$  the time elapsed since the beginning of the simulation until the secondary is totally destroyed. After that, the amplitude of the gravitational wave decays to zero. The product of the Fourier transform of the dimensionless strains and the square root of the frequency,  $\tilde{h}(f)\sqrt{f}$ , can then be compared with the noise curves of the gravitational-wave detectors ALIA and eLISA. The signal-to-noise-ratios (SNR) were computed as in [Giacomazzo et al. 2011]:

$$(SNR)^2 = 4 \int_0^{\infty} \frac{|\tilde{h}(f)|^2}{S_n(f)} df \quad (28)$$

where  $S_n(f)$  is the power spectral density of the detector.

### 3.2.2. Thermal neutrinos

Neutrino emission is computed taking into account the five traditional neutrino processes such as electron-positron annihilation, plasmon decay, photoemission, neutrino bremsstrahlung, and neutrino recombination [Itoh et al. 1996]. To assess the possibility of detecting some of the emitted neutrinos, the prescriptions of [Odrzywolek & Plewa 2011; Kunugise & Iwamoto 2007] were followed. Specifically, the expected number of neutrino events that could be detected in the Super-Kamiokande detector, when the source is at a distance of 1 kpc, were computed.

To achieve this, firstly the neutrino spectral flux was computed

$$\Phi(E_\nu, t) = \frac{L}{A\langle E_\nu \rangle^4} \frac{aE_\nu^2}{1 + \exp\left(\frac{bE_\nu}{\langle E_\nu \rangle}\right)} \quad (29)$$

where  $L$  is the neutrino luminosity at time  $t$ ,  $A$  is the irradiated area at a distance  $d$ ,  $\langle E_\nu \rangle = 3.15137T_\nu$  is the average neutrino energy at time  $t$ ,  $T_\nu$  is the maximum temperature at time  $t$ ,  $a \cong 17.3574$  and  $b \cong 3.15137$ . The neutrino luminosity and the maximum temperature at time  $t$  were obtained from the SPH simulations. Assuming energy equipartition between all the emitted neutrino flavours, the number of detectable events can be approximated by estimating the rate of electron-neutrino neutrino scattering. The cross section of this scattering depends on the threshold energy of recoil electrons,  $T_e^{\text{th}}$ :

$$\sigma(E_\nu, T_e^{\text{th}}) = \frac{\sigma_0}{m_e} \left[ \begin{aligned} & (g_1^2 + g_2^2)(T_e^{\text{max}} - T_e^{\text{th}}) \\ & - \left( g_2^2 + g_1g_2 \frac{m_e}{2E_\nu} \right) \left( \frac{T_e^{\text{max}^2} - T_e^{\text{th}^2}}{E_\nu} \right) \\ & + \frac{1}{3} g_2^2 \left( \frac{T_e^{\text{max}^3} - T_e^{\text{th}^3}}{E_\nu^3} \right) \end{aligned} \right] \quad (30)$$

where  $\sigma_0 \cong 88.06 \times 10^{-46} \text{cm}^2$ ,

$$T_e^{\text{max}} = \frac{2E_\nu^2}{m_e + 2E_\nu} \quad (31)$$

the maximum kinetic energy of the recoil electron at a neutrino energy  $E_\nu$ ,  $g_1 \cong 0.73$  and  $g_2 \cong 0.23$ . Then, the total number of neutrino events is given by

$$N = nV \int F_\nu(E_\nu) \sigma(E_\nu, T_e^{\text{th}}) dE_\nu \quad (32)$$

where  $n$  and  $V$  correspond to the number density of electrons and volume of water in the tank of the Super-Kamiokande detector, respectively, and  $F_\nu$  is the time-integrated spectrum.

### 3.2.3. Fallback X-ray luminosity

Another possible observational signature of the coalescence of two white dwarfs is the emission of high-energy photons from the fallback material in the aftermath of the merger. During the merger, the less massive star is disrupted and its material is accreted into the more massive white dwarf. This material forms a disk, where the vast majority of the gas follows circularized orbits. However, some of the particles have highly eccentric orbits and after some time, this material interacts with the rest of the disk.

Using the approach described in [Rosswog 2007], the fallback accretion luminosities can be computed. This approach assumes that the kinetic energy of particles with a high eccentric orbit is dissipated within the radius of the disk. Particles launched into eccentric orbits, but still bound to the remnant, are treated as point-like masses in the gravitational field of the enclosed mass  $M$ . It is also assumed that the hydrodynamic pressure forces can be neglected, and the dynamics follows a point-mass two-body problem between the particle and the enclosed mass. Consequently, for each particle, the angular momentum  $L$  and energy  $E$  can be easily estimated. Then, the orbital eccentricity and semi-major axis can be expressed as

$$e_i = \sqrt{1 + \frac{2E_i J_i^2}{G^2 m_i^3 M^2}} \quad \text{and} \quad a_i = -\frac{GMm_i}{2E_i}. \quad (33)$$

The maximum and minimum orbital distances with respect to the origin will be then give, for each particles, by

$$r_{\max,i} = a_i(1 + e_i) \quad \text{and} \quad r_{\min,i} = a_i(1 - e_i) \quad (34)$$

Consequently, the radial velocity of the particles is

$$\frac{dr}{dt} = \pm \sqrt{\frac{2}{m_i} \left[ E_i - V(r) - \frac{J_i^2}{2m_i r^2} \right]} \quad (35)$$

where  $V$  is the potential energy of the two-body problem and the positive/negative sign refers to a motion away from/towards the origin.

Then, the time it takes a particle to move from a radius  $r_1$  to a radius  $r_2$  can be written as

$$\tau_{r_1, r_2} = \pm \int_{r_1}^{r_2} \frac{r \, dr}{\sqrt{Ar^2 + Br + C}} \quad (36)$$

where  $A = 2E_i/m_i$ ,  $B = 2GM$  and  $C = -J_i^2/m_i^2$ . The integral can be analytically solved, and by replacing  $r_1$  and  $r_2$  by  $r_i$  and  $R_{\text{disk}}$  respectively, the fallback accretion time can be found.

Since it is assumed that all the energy is dissipated when a particle reach the disk radius, the fallback energy  $E_{\text{fb}}$  turns out to be the difference between the potential plus kinetic energy at the start radius  $r_i$ , and the potential energy at the disk radius  $R_{\text{disk}}$ .

Finally, the fallback accretion luminosity can be written as

$$L_{\text{fb}} = -\frac{E_{\text{fb}}}{\tau_{r_i, R_{\text{disk}}}} \quad (37)$$

# 4. RESULTS

In this section, the main results of the numerical simulations performed here are presented. The section is organized as follows, in Sects. 4.1 to 4.5 the results of the different calculations are discussed. In order to illustrate the main characteristics of the merging process, the 0.3+0.6 (HR) simulation will be used through the section. However, we explicitly mention that the results of all other simulations are similar. In Sect. 4.6, a description of the potential observational signatures of the merger is presented.

## 4.1. Time evolution of the merging process

During the initial phases of the merging process, the secondary star is tidally deformed by the gravitational force of the primary star until it overflows its Roche Lobe. Its material is subsequently accreted onto the primary star, forming an accretion disk around it. This is due to angular momentum conservation. After some time, the secondary star is completely disrupted and falls towards the primary white dwarf. The resulting final configuration consists of a central compact object, surrounded by a hot, rapidly rotating corona, and an accretion disk with a quasi Keplerian rotational profile. Moreover, some particles are not in the disk but they form a debris region in the outermost regions. In Fig. 3 some snapshots of the merging process are presented for the 0.3+0.6 (HR) solar masses case, whereas in the panels of Fig. 4 the angular velocity profile of the final remnant is presented, clearly illustrating the four different regions of the merged configuration.

A common feature of binary mergers of white dwarfs is the formation of a hot corona of material around the primary white dwarf. The first material falling onto the primary white dwarf is heavily compressed, and is heated sizably. This leads to the formation of a hot corona around the primary star, as it can be clearly appreciated in the lower panels of Fig. 3, and in the panels of Fig. 4. This region has been found in many previous simulations in the literature, and plays a crucial role in the future evolution of the merged configuration [Lorén-Aguilar et al. 2009]. It is in this region where the highest temperature is achieved and the region where nuclear reactions will mainly take place (see Sect. 4.5 for a detailed discussion).

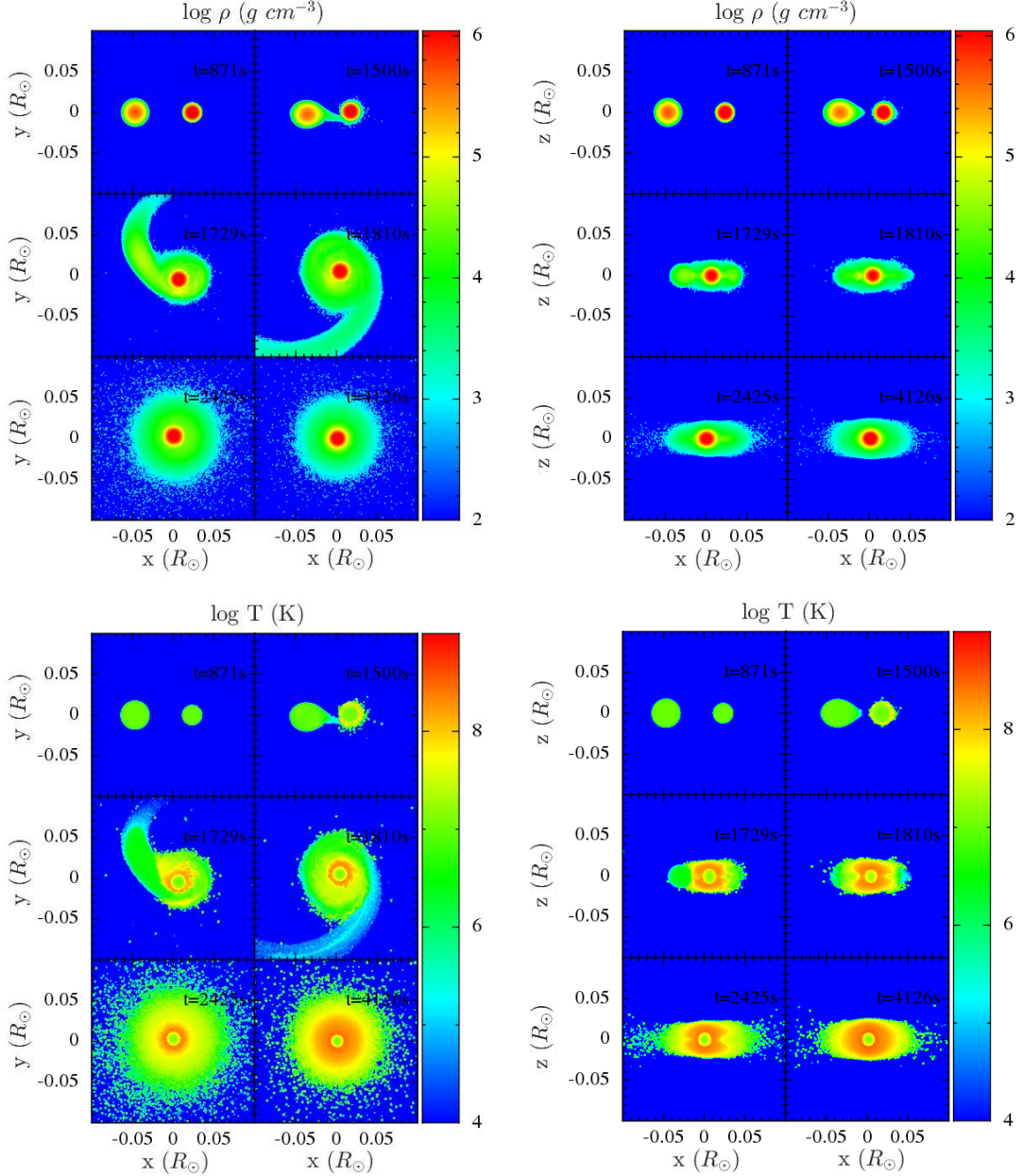


**Figure 3.** Temporal evolution for the coalescence of the 0.3+0.6 (HR) solar masses simulation. The top panels correspond to the logarithmic density profile in the equatorial (*left panels*) and the polar (*right panels*) planes, whereas the bottom panels correspond to logarithmic temperature profile in the equatorial (*left panels*) and the polar (*right panels*) planes. Time is shown in the right upper corner of each panel.

There is also a debris region surrounding the disk formed by particles that have been ejected from it. The physical soundness of this debris region must be considered with some caution, since they are moving away from the disk and, more importantly, they are close the minimum density threshold set in the code. In any case, these particles are gravitationally bound, and will fall back into the remnant, being incorporated into the disk.

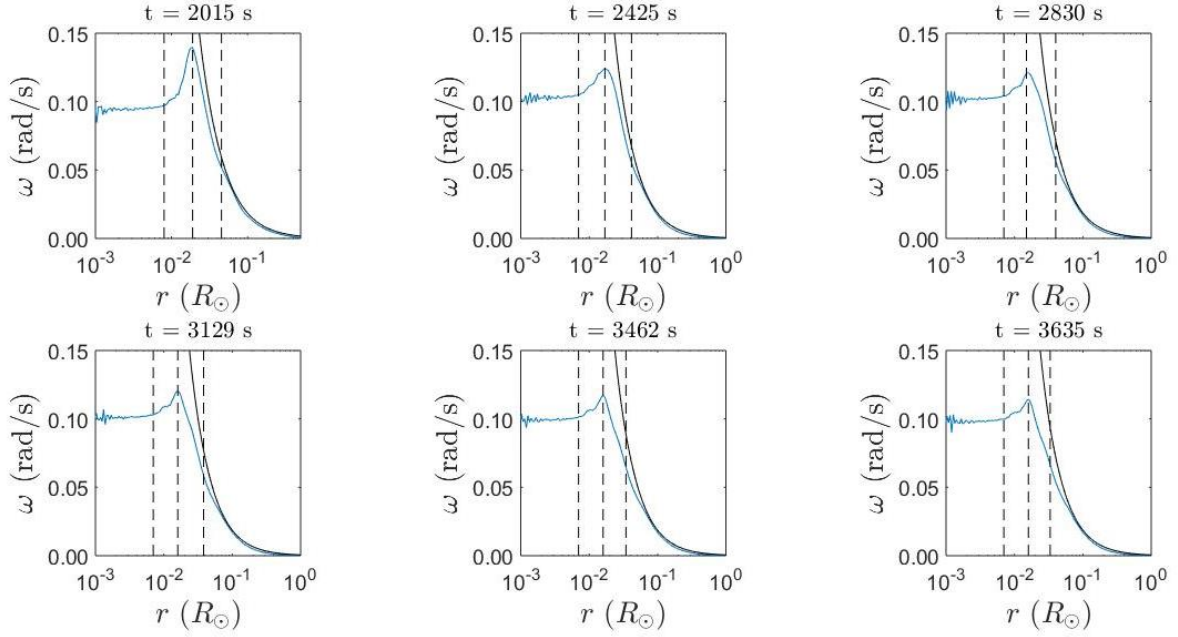


**Figure 4.** Angular velocity profile of the merger products of the 0.3+0.6 (HR) solar masses simulation as a function of the radius at different times. For the sake of comparison the Keplerian velocity is also shown as a solid black line. The external radii of the compact object, the hot corona and the disk, from left to right, are represented by dashed lines.

## 4.2. Definition of the radii of the merger remnant

The outer edges of each of the regions previously described are defined next and shown in Fig. 5.

### 4.2.1. Central object

In this work we have assumed that all the less massive white dwarfs have a pure helium core, whereas the more massive ones have a carbon-oxygen core. Hence, the easiest way to locate the radius of the compact object is to search for the radius where a significant increase of helium is found.

### 4.2.2. Corona

The external radius of the hot corona is defined as the radius where the angular velocity and temperature reach their maximum.

### 4.2.3. Accretion disk

The external radius of the disk is located at the position where the density of the particles reaches the minimum threshold set in the code. Such a threshold is set in order to prevent particles from achieving spuriously high velocities due to pure numerical effects,

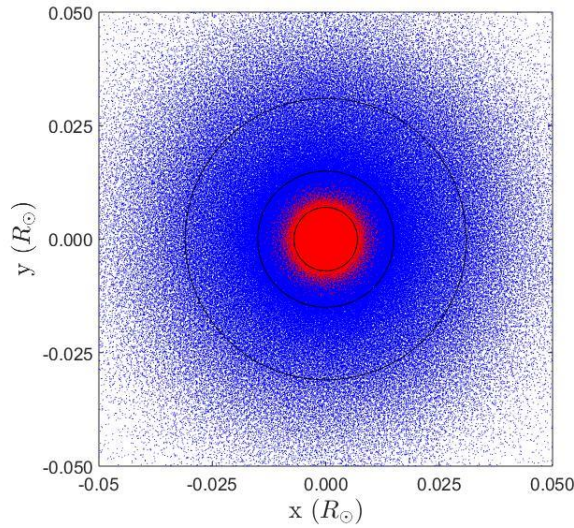


**Figure 5.** Scheme of the different regions of the remnant after the merger. The particles of the more massive star are represented in red whereas the particles of the less massive one are represented in blue. Moreover, the external radii of the compact object, the hot corona and the disk, from the center to outside, are shown by solid black lines.

like a small number of neighbors. This guarantees numerical stability in low-density regions.

### 4.3. Characteristics of the merger remnant

In Table 1, the main characteristics of the final remnant of each simulation are presented. Paying attention to the radius of the compact object, it can be seen that the primary star reduces its radius due to the accreted material from the secondary white dwarf (as one would expect for a degenerate object). The external radius of the hot corona also depends on the total mass of the coalescence, being closer to the central object when the total mass of the system increases.

It can also be seen how the radius of the disk depends of the mass of the system. For simulations with a primary star with a mass of 0.6 solar masses, the smaller the mass of the less massive star is, the smaller the disk radius is. The 0.3+1.0 solar masses simulation has a radius of 0.043 solar radii, due to the increased mass of the primary. Hence, there is dependence between the total mass of the merger and the disk radius. Furthermore, the change of resolution in the 0.3+0.6 simulation only affects the central object radius, becoming smaller due to the reduction of particles in the more massive white dwarf.

Run	$R_{\text{wd2}}$	$R_{\text{co}}$	$R_{\text{corona}}$	$R_{\text{disk}}$	$T_{\text{peak}}$	$r_{\text{peak}}$	$T_{\text{disk}}$
0.2+0.6	0.013	0.0093	0.016	0.024	$3.46 \times 10^8$	0.01040	$2.13 \times 10^8$
0.3+0.6	0.013	0.0081	0.015	0.029	$3.12 \times 10^8$	0.00945	$1.96 \times 10^8$
0.4+0.6	0.013	0.0082	0.014	0.044	$2.03 \times 10^8$	0.00861	$7.09 \times 10^7$
0.3+1.0	0.008	0.0065	0.013	0.043	$6.77 \times 10^8$	0.00723	$1.99 \times 10^8$
0.3+0.6 (HR)	0.011	0.0070	0.015	0.031	$3.15 \times 10^8$	0.00876	$1.71 \times 10^8$

**Table 1.** Properties of the remnant at the end of the coalescence. The radii are expressed in solar units and temperature in K.

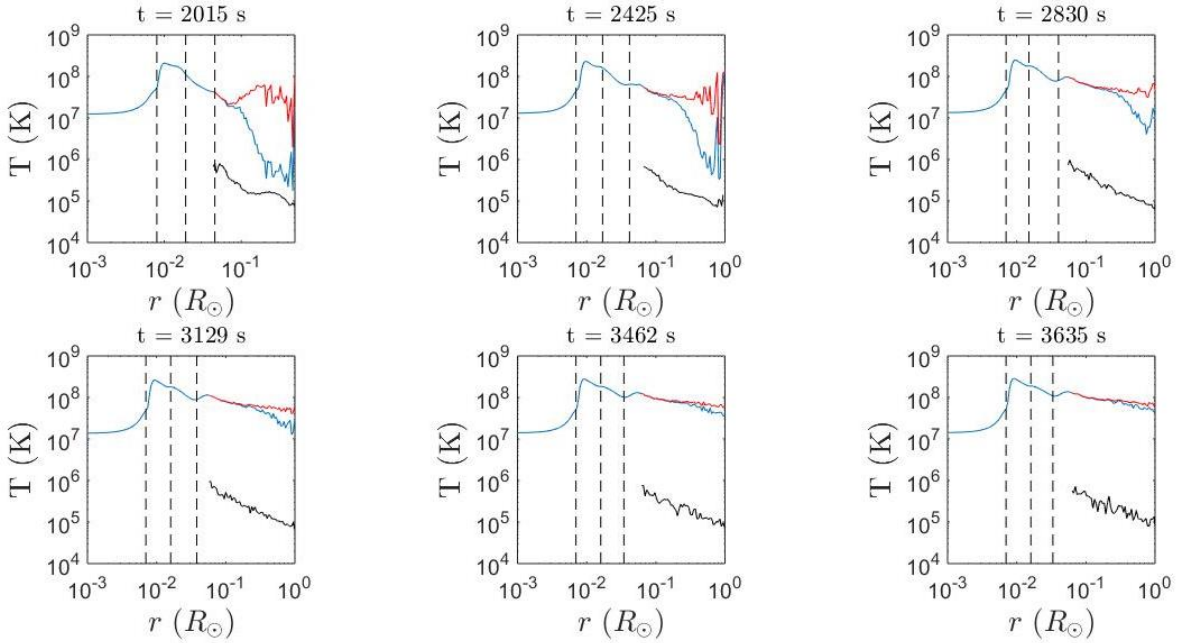


**Figure 6.** Temperature profile of the merger products of the 0.3+0.6 (HR) solar masses simulation as a function of the radius at different times. The temperature of the tidal stream and the debris are represented by a solid black and red line, respectively. The external radii of the compact object, the hot corona and the disk, from left to right, are represented by dashed lines.

It is also evident that the temperature profile of the merger remnant depends as well on the stellar masses. The higher the mass difference between the primary and secondary star, the highest the maximum temperature in the corona is. This was again a foreseeable result, since the kinetic energy of the particles accreted onto the primary white dwarf strongly depends on the mass difference between the stars.

In Fig. 6, the time evolution of the temperature profile of the 0.3+0.6 (HR) solar masses case is shown, as a representative example. The various different regions previously discussed can be clearly seen as well in the temperature profile of the remnant (blue line).

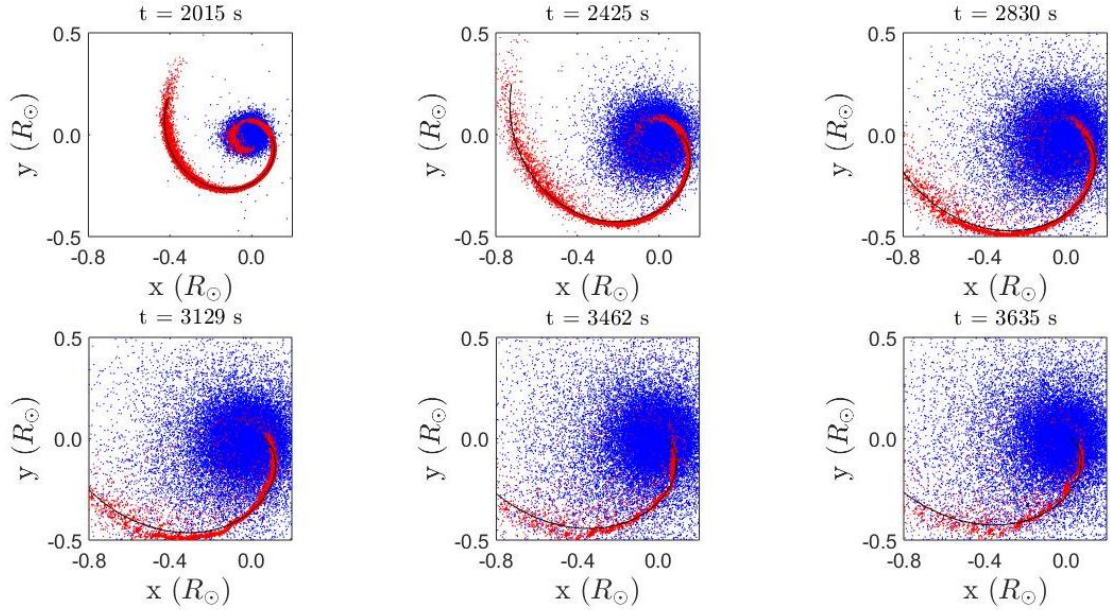


**Figure 7.** Temporal evolution of the tidal stream of the 0.3+0.6 (HR) solar masses simulation, represented in red. For sake of comparison, the disk and the debris are represented in blue. The averaged stream position is represented by a solid black line.

In the central region of the remnant we find the primary white dwarf, which keeps its initial temperature ( $T \sim 10^7$  K) despite the merging process. Surrounding the primary star, we find the aforementioned hot corona, with temperatures well above  $10^8$  K, and beyond that, we find the rapidly rotating disk.

It is also interesting to note that, in the last phases of the merging process, a tidal stream is formed when the secondary star becomes completely disrupted (see Fig. 7 for an illustration). The temperature profile of such stream is represented by the black line. Because the stream is formed from expanded regions of the secondary star, it has significantly cooled down. Finally, in the outermost region, there are also some particles that were ejected during the merging process, that form a disperse halo around the remnant (red line). Those particles were ejected from the innermost regions of the merger, and are considerably hot. However, as time goes by, they clearly cool down. Also, it is interesting to note that as the merger evolves, a local minimum in the disk temperature appears. This minimum is located at the contact point between the disk and the tidal stream, and is caused by the mixing of cold particles coming from the stream with the hotter disk material.

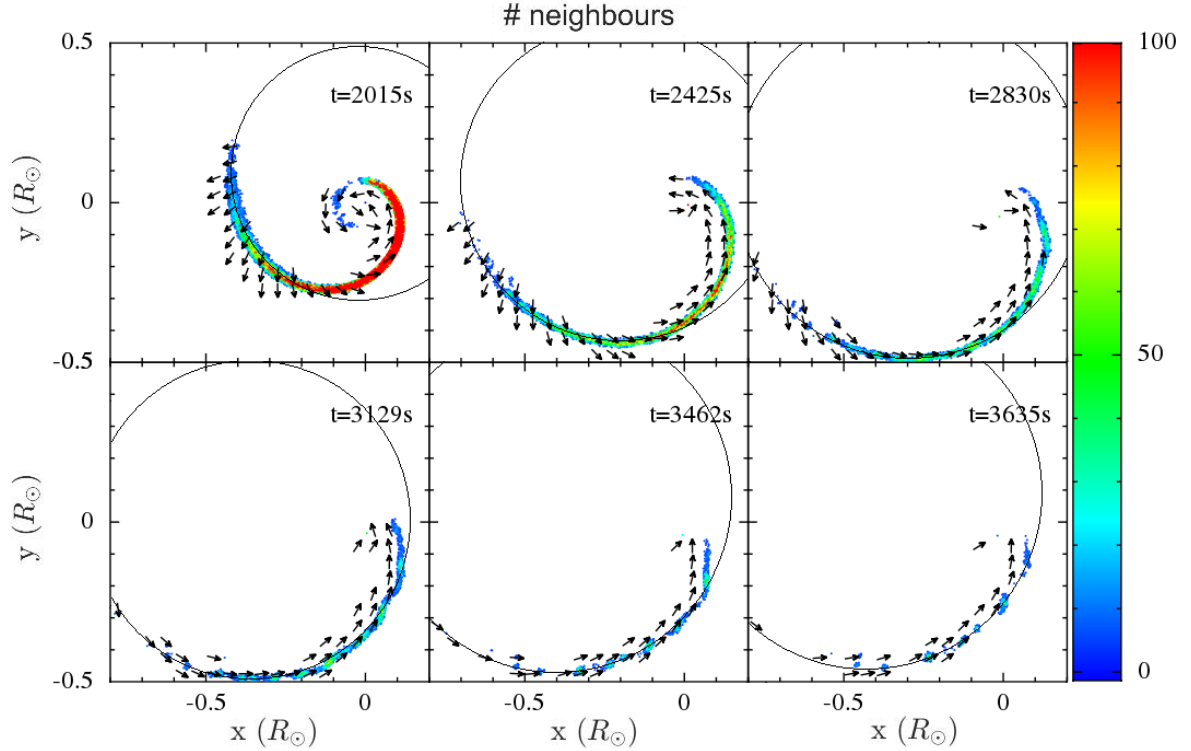


**Figure 8.** Temporal evolution of the position and velocity of the tidal stream of the 0.3+0.6 (HR) solar masses simulation. The osculating circle of the tidal stream is shown as a black solid line and the direction of the velocity field of the stream is represented by black arrows. The number of neighbours of each particle has been rendered.

#### 4.4. Evolution of the tidal stream

As previously mentioned, in all the simulations the secondary star forms a tidal stream during the merging process. Due to the gravitational pull produced by the primary star, the less massive white dwarf becomes thinner and elongated with time, forming a characteristic arm.

Fig. 7 shows the tidal stream particles (red particles), the averaged stream position (black solid line), and the accretion disk and debris particles (blue particles) as a function of time. To study the velocity profile of the arm, we must first locate its position. To do this, the osculating circle (circle that best fits a curve) of the tidal stream is calculated and compared with its velocity field. By inspecting Fig. 8, it can be seen how, initially, the particles of the tidal stream had a quasi-radial velocity with respect to the averaged tidal stream. However, as the curvature of the tidal stream increases, the velocity becomes tangent to it and the size of the circle becomes stable. Note that this change in velocity is progressively made, starting in the region that is closer to the center of masses. The curvature radius of the tidal stream is the same as the radius of the osculating circle, and it reaches 1.1 solar radii in this case. At this moment, the velocities of the particles

are tangent to that circle and they start to fall following the osculating circle. The length of the steady radius is related with the difference between star masses, being larger for higher difference between white dwarf masses. This simply evidences the fact that the particles of the stream are gravitationally bounded, and are due to fall towards the remnant. This is also confirmed by the fact that the total mechanical energy of the stream is negative, evidencing gravitational binding.

Also, during the analysis of the evolution of the stream, an interesting feature was observed. The tidal stream showed evidence of fragmentation in small clumps of particles, before all of its mass was accreted onto the disk. This has been unreported previously, and it was unexpected. Hence, a careful analysis was made. After analyzing the velocity profile of the particle field, the presence of any self-gravitating fragmentation was discarded, since the particles strictly followed the stream without showing any evidence of local collapse (i.e. particles moving towards each other). Moreover, since the density and temperature of the stream are close to uniform, any compositional effect can be the responsible. As previously mentioned, the code has a minimum density threshold in density, in order to prevent numerical noise in the scattered particles around the merger. Hence, the changes in density, sound speed and temperature for the tidal stream particles are extremely small. As a consequence, there are no pressure inhomogeneities capable of explaining the clumps. However, by plotting the number of neighbors for each particle (color rendering in Fig. 8), one can easily see the presence of the clumps.

## 4.5. Abundance profiles

In Fig. 9, the time-evolution of the radial profile of the abundances for several different chemical elements is shown for the 0.3+0.6 (HR) solar masses simulation. As it can be expected, the center of the remnant is made of 40% of carbon and 60% of oxygen, because it is the composition of the primary star.

Surrounding the central object, there is a hot corona made of a mixture of He, coming from the secondary star, and C and O coming from the primary. As time passes by, the abundance of heavier elements in this region increases. Elements such as Ne, Mg or Si are produced due to the nuclear reactions caused by the high temperatures achieved during the merger.

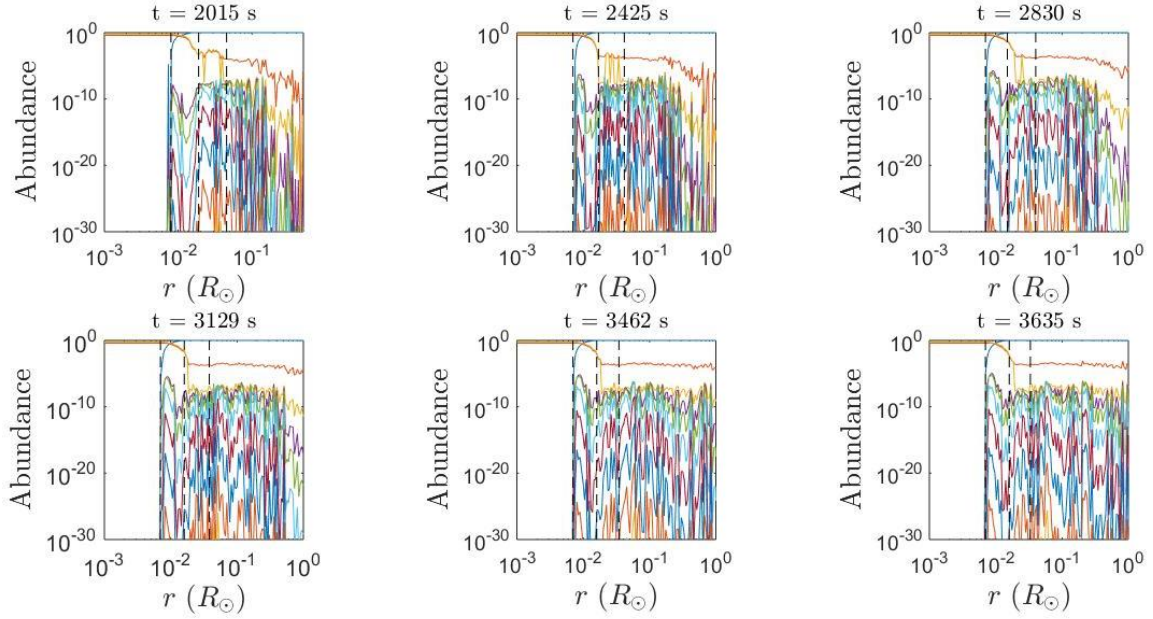


**Figure 9.** Abundance profile of the merger products of the 0.3+0.6 (HR) solar masses simulation as a function of the radius at different times. The external radii of the compact object, the hot corona and the disk, from left to right, are represented by dashed lines. The blue line corresponds to He, the red one to C, the yellow one to O, the purple one to Ne, the green one to Mg, the light blue one to Si and the magenta one to S.

The disk, that surrounds the hot corona, is mainly made of helium, carbon and oxygen. The majority of the disk is made of helium, because almost all its particles came from the secondary white dwarf, and there is not enough temperature in the disk to start nuclear reactions. There is a significant amount of carbon particles, coming from the secondary star, which have been synthesized in the hot corona and pulled out during the merger. Since carbon is synthesized at a lower temperature than the rest of the heavier elements, there is a bigger carbon to oxygen ratio outside the compact object.

The outermost zone has approximately the same composition than the disk. The tidal stream, made of pure He, and the debris coming from the disk are located in this region. In the outermost regions of the remnant the values of the elements heavier than C fluctuate considerably. These fluctuations are produced due to the very small number of particles present, and must be interpreted as numerical noise. However, in order to compare the results of the different simulations, Tables 2 and 3 display the averaged abundances of various elements in each region of the merger at the end of the simulations, as well as the carbon-oxygen ratio. The abundance of the tidal stream is not shown because it is almost completely made of He, the composition of the secondary white dwarf. This occurs because the tidal stream does not have a temperature large enough to burn He.

Run	He	C	O	Ne	Mg	Si	S	C/O
0.2+0.6	0.95	0.019	0.029	2.7E-14	5.2E-18	2.6E-24	1.5E-32	0.67
0.3+0.6	0.91	0.033	0.049	1.9E-9	6.9E-10	1.9E-11	3.3E-15	0.67
0.4+0.6	0.93	0.027	0.041	1.1E-7	2.2E-7	1.3E-7	6.8E-10	0.68
0.3+1.0	0.97	0.020	0.003	5.2E-5	9.7E-5	2.4E-5	1.8E-6	8.09
0.3+0.6 (HR)	0.99	0.001	0.001	1.1E-8	6.4E-9	6.6E-10	5.9E-13	0.98

**Table 2.** Averaged abundances (mass fraction) of He, C, O, Ne, Mg, Si and S of the hot corona region obtained by the end of the coalescing process.

Run	He	C	O	Ne	Mg	Si	S	C/O
0.2+0.6	0.75	0.12	0.12	4.5E-8	7.0E-10	7.0E-14	7.1E-20	0.98
0.3+0.6	0.72	0.13	0.14	3.0E-11	6.1E-15	1.9E-21	1.3E-29	0.91
0.4+0.6	0.63	0.15	0.22	9.4E-10	7.3E-11	1.3E-13	1.6E-18	0.67
0.3+1.0	0.55	0.35	0.01	2.7E-3	1.7E-2	2.3E-2	2.9E-4	6.32
0.3+0.6 (HR)	0.44	0.25	0.31	7.9E-6	4.2E-6	8.7E-8	1.9E-11	0.79

**Table 3.** Averaged abundances (mass fraction) of He, C, O, Ne, Mg, Si and S of the accretion disk region obtained by the end of the coalescing process.

As previously said, the corona is made of a mixture of the helium-rich material of the secondary star, the carbon and the oxygen material coming from the primary star, and some carbon synthesized by helium burning reactions during the merger. There are also various different heavier elements in the remnant, but their percentage in mass is very small, with the exception of the 0.3+1.0 solar masses simulation, where Ne, Mg, Si and S have higher relative abundances, when compared with the rest of the simulations. This simulation is the most energetic one, and the temperature of the corona is the hottest.

Note that for the cases in which 0.2+0.6, 0.3+0.6 and 0.4+0.6 binary systems are computed, which all have the same primary white dwarf, the amount of helium decreases when the difference between the two masses does. The larger the contrast of stellar masses is, the highest the energy of accreted particles is, and therefore more helium can be found in the hot corona. It is interesting note that the results of simulation 0.3+0.6 (HR) noticeably differ from the ones in simulation 0.3+0.6. This suggests that, unlike the hydrodynamical evolution, the chemical evolution is way more sensitive to the numerical resolution, and hence its results must be interpreted with caution.

We now discuss the carbon-oxygen ratio. Those simulations with higher temperatures in the corona show higher ratios, having all of them higher ratios than the primary star, which is 0.66. This was expected, since the only mechanism to produce carbon is by burning He, and all simulations produce more carbon than oxygen. Moreover, the amount of He is lower than the expected one, meaning that it has

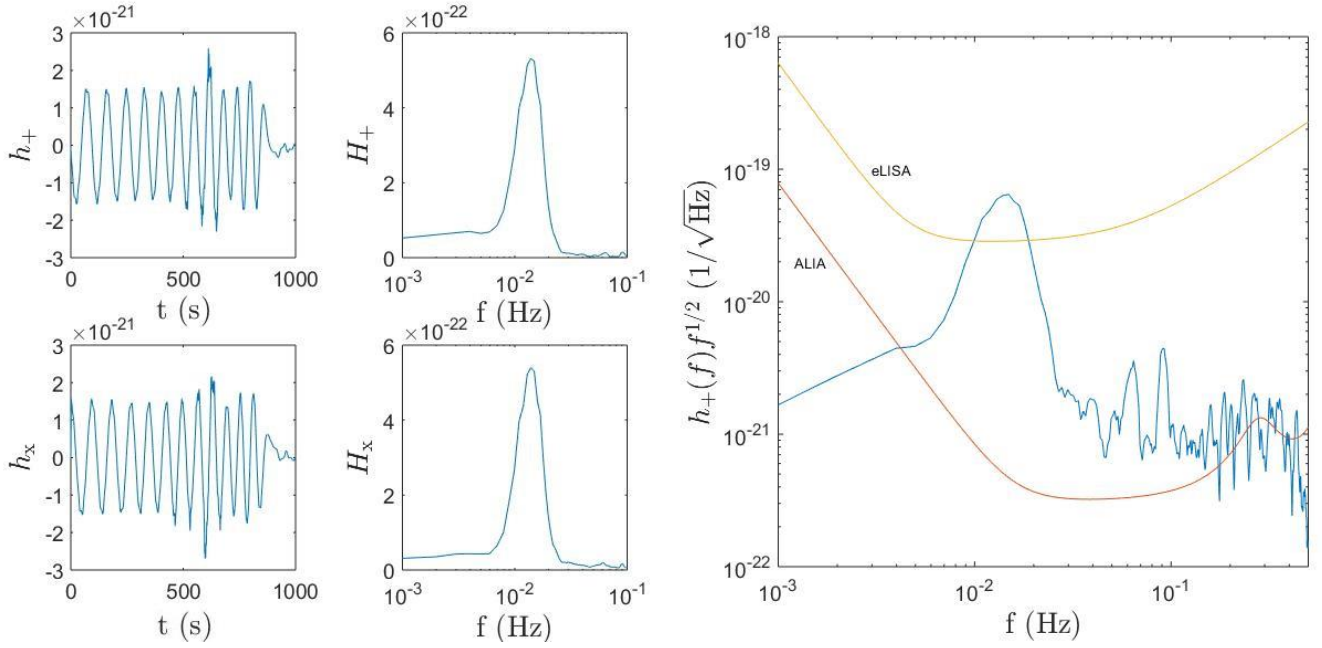


**Figure 10.** The plus and cross polarization of gravitational waves (left panels) as well as its Fourier transforms (center panels) of the 0.3+0.6 (HR) solar masses simulation. The Fourier signal is compared with the sensitivity curves of eLISA and ALIA in the right panel. These signals are obtained for  $i=0$  degrees and a distance of 10 kpc.

been burned and transformed primarily into carbon. This deficit becomes larger as the temperature of the corona increases.

Regarding the disk composition, it can be seen in Table 3 that for the simulations of 0.2+0.6, 0.3+0.6 and 0.4+0.6 solar masses, the carbon-oxygen ratio is approximately equal to the one in the primary white dwarf. This happens because the primary white dwarf is spread throughout the disk.

## 4.6. Observational signatures of the merger

In addition, some observational features of the merger are studied such as the gravitational waves, the light curves, the expected thermal neutrino events, the fallback X-ray luminosities and the optical densities. Those results are shown next.

### 4.6.1. Gravitational waveforms

The gravitational waveforms and its dimensionless Fourier transforms in both polarizations are calculated for a face-on orbit, as explained in Sect. 3.2.1, and compared with two detectors (eLISA and ALIA) in order to know if the radiated waves could be detected on Earth. As it can be seen in Fig. 10, before the merger occurs, both polarizations of the gravitational waves (left panels)

Run	$\Delta t$	$A_0$	$E_{GW}$	$f_{\max}$	$f_0$	SNR	
						eLISA	ALIA
0.2+0.6	400	$1.8 \times 10^{-21}$	$3.5 \times 10^{41}$	0.009	0.0048	0.76	28.7
0.3+0.6	900	$1.6 \times 10^{-21}$	$6.2 \times 10^{41}$	0.013	0.051	1.28	66.8
0.4+0.6	920	$1.5 \times 10^{-21}$	$8.6 \times 10^{41}$	0.017	0.054	9.30	642.1
0.3+1.0	700	$1.0 \times 10^{-20}$	$2.6 \times 10^{43}$	0.013	0.061	47.52	24206
0.3+0.6 (HR)	1000	$1.6 \times 10^{-21}$	$9.5 \times 10^{41}$	0.014	0.051	1.51	85.8

**Table 4.** Properties of the gravitational wave emission. Time is expressed in seconds, the energy in erg and the frequencies in  $\text{s}^{-1}$  for the plus polarization,  $i=0$  degrees and a distance of 10 kpc.

have a nearly sinusoidal shape, and their dimensionless Fourier transform (center panels) are almost monochromatic.

Its peak is twice the orbital frequency, as it can be expected in binaries systems in circular orbits. Note that the amplitude of the gravitational waves decreases as time passes by. This is a consequence of the fact that there are several mass transfer episodes during that period of time, and the orbit is slightly modified. After some mass transfers, the less massive star is totally destroyed, leading to a merger.

At this point, the system becomes almost completely symmetric, and the amplitude of gravitational waves decays to zero. As can be seen in the left panels of Fig. 10, there is still a small emission after the merger takes place, caused by some small oscillations of the remnant.

In Table 4, the properties of the gravitational waves emitted in each simulation is presented for each simulation: the duration of the emission of gravitational, the initial amplitude  $A_0$ , the energy radiated by the wave, the frequency of the peak, the initial orbital frequency and the signal-to-noise ratio for the plus polarization, where an inclination of zero degrees and a distance of 10 kpc have been assumed. It is interesting to realize that the more massive the secondary white dwarf is, the longer the merger is (assuming we have the same primary star). It is also worth noting that the higher the difference between the stellar masses is, the higher the amplitudes of gravitational waves. The total energy radiated by the wave depends on the duration of the mass transfer and the amplitude of the wave.

It is worth mentioning that we detected a small bug was in the SPH code thanks to the calculation of the gravitational wave emission. Each time the simulation was restarted, a slightly wrong value for the thermal energy of the stars was used. This caused a small unbalance in the hydrostatic equilibrium of the stars, inducing small pulsations. This effect has almost no effect

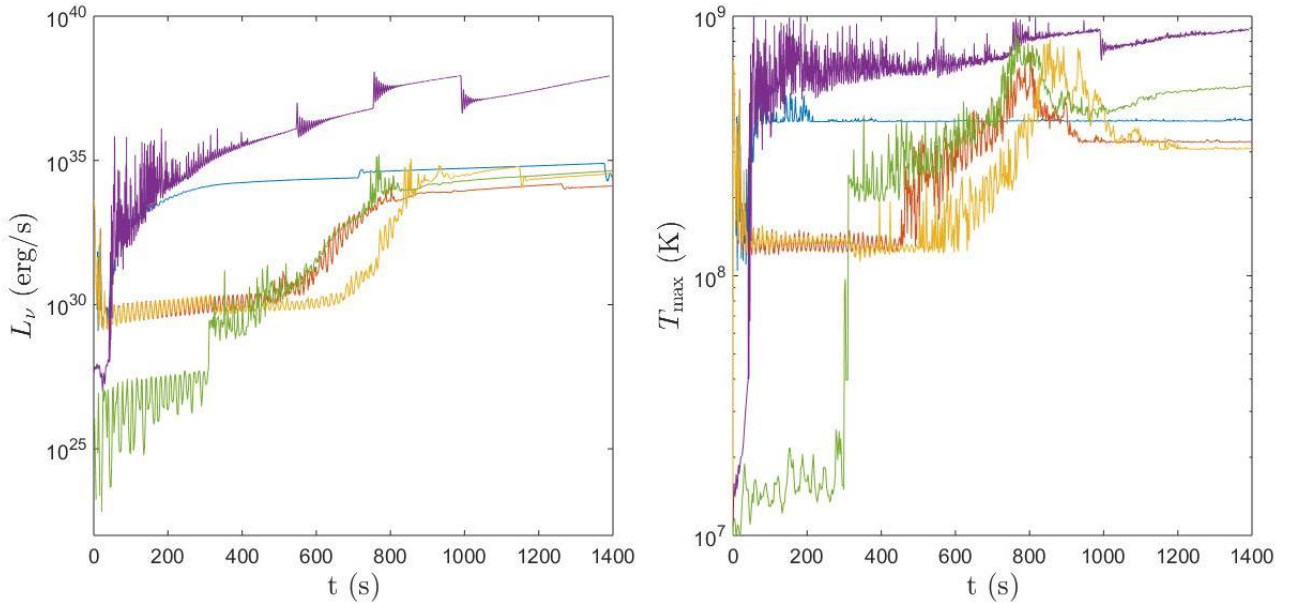


**Figure 11.** Thermal neutrino luminosity (left panel) and maximum temperature achieved (right panel) as a function of time. The simulation of the 0.2+0.6 system is represented by a blue line, the simulation of the 0.3+0.6 binary by a red one, the simulation of the 0.4+0.6 pair by a yellow one, the 0.3+0.1 run by a purple one and the simulation 0.3+0.6 (HR) by a green one.

in the hydrodynamical evolution of the merger, and hence remained undetected.

However, it was detectable in the gravitational wave emission, since induced a small bump in the emission for some of the simulations. The simulations for 0.3+0.6, 0.4+0.6 and 0.3+1.0 systems were restarted during the mass transfer episodes, and the gravitational waves were slightly affected by this bug. For this reason, the results of the power radiated and the SNR of those simulations must be interpreted with some caution.

Finally, in the right panel of Fig. 10, the sensitivity curve of eLISA and ALIA, and the product of the plus polarized gravitational wave with the square root of the frequency that would be detected in the equatorial plane at a distance of 10 kpc are presented. As can be seen in Table 4, both systems should be able to detect all the gravitational waveforms, except the first one (0.2+0.6 solar masses), which cannot be detected by eLISA. Despite having this case the highest gravitational wave amplitude of all the simulations with a 0.6 solar masses primary star, the orbital frequency results too small to be detected.

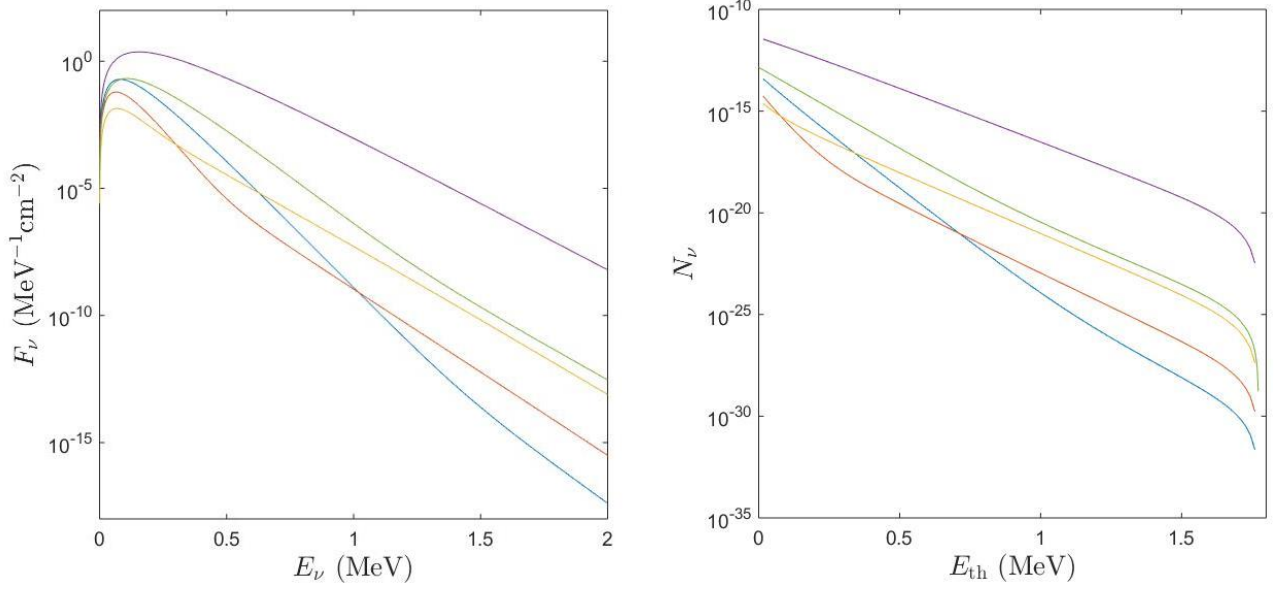


**Figure 12.** Spectral energy distribution as a function of neutrino energy (left panel) and expected number of thermal neutrino events as a function of the threshold energy in the Super-Kamiokande detector (right panel) when the source is located at 1 kpc. The colour coding is the same as in Fig. 10.

#### 4.6.2. Neutrinos

The neutrino emission rate is computed in each simulation and presented in the left panel of Fig. 11 as a function of time. It is interesting to compare the neutrino emission with the maximum temperature (right panel of Fig. 11). At the beginning, both luminosity and maximum temperature oscillate. This corresponds to the spiraling phase of the white dwarf merger. This phase is different for each simulation, being shorter in the 0.2+0.6 and 0.3+1.0 solar masses runs. When the mass transference starts, the luminosity and the temperature increase until the secondary white dwarf is disrupted. The helium accreted into the more massive star is compressed, and therefore the temperature rises. When the secondary star is disrupted, the accreted mass rate decreases and thus the temperature of the hot corona decreases and becomes stable except in simulation 0.3+1.0). By inspecting both figures, it can be seen that there is clear correlation between temperature and thermal neutrino rate, as it should be expected. Moreover, it can be seen the aforementioned bug in the light curve of simulation 0.3+1.0 run.

The spectral energy distribution (left panel) and the expected number of thermal neutrino events (right panel) in the Super-Kamiokande detector is presented in Fig. 12 for all simulations. As a reference, we have assumed a distance to the source of 1 kpc (see Sect. 3.2.2 for details). As can be seen in the left panel of Fig. 12, all the simulations show a maximum at small energies, between 0.06 and 0.15 MeV.

Run	$E_\nu$
0.2+0.6	$1.8 \times 10^{38}$
0.3+0.6	$3.7 \times 10^{37}$
0.4+0.6	$1.1 \times 10^{37}$
0.3+1.0	$8.1 \times 10^{39}$
0.3+0.6 (HR)	$3.5 \times 10^{38}$

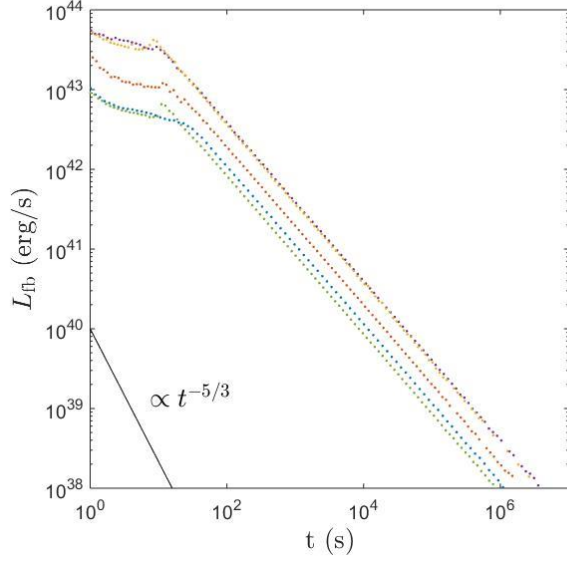


**Table 5.** Total energy radiated as thermal neutrinos during the coalescence. The energy is expressed in erg.

**Figure 13.** Fallback accretion luminosity of each simulation. A straight line with slope  $-5/3$  is shown for the sake of comparison. The color coding is the same as in Fig. 10.

Thermal neutrino emission is closely related to the maximum temperature achieved during the merging process. Comparing all the simulations with a primary star of 0.6 solar masses, the larger the difference between the masses is, the higher the energy at which the peak is located. The case of simulation 0.3+1.0 solar masses, which is the most asymmetric, has the highest energy peak at 0.15 MeV. Note that at lower energies, the simulations of 0.3+0.6 solar masses (yellow and green lines) has different distributions, but for higher energies, the distributions converge.

As expected, the 0.3+1.0 simulation has the higher number of expected thermal neutrinos. In Table 5, the radiated thermal neutrino energy is shown for each simulation.

#### 4.6.3. Fallback luminosity

Fig. 13 shows the fallback accretion luminosity curve for each simulation, computed accordingly with Sect. 3.2.3. It is important to note that the slope of accretion fallback luminosities differ from the canonical value  $\propto t^{5/3}$ . In fact, the result of the fallback luminosity is approximately  $\propto t^1$ . In the analytical model, the central object is a black hole, whereas in this work, is a white dwarf. There are two parameters involved in the assumptions: the mass of the central object and the geometry of the disk. The second parameter only affects the energy radiated, whereas the mass of the central object affects the slope of the fallback luminosity. For that reason, the fallback luminosity has to be

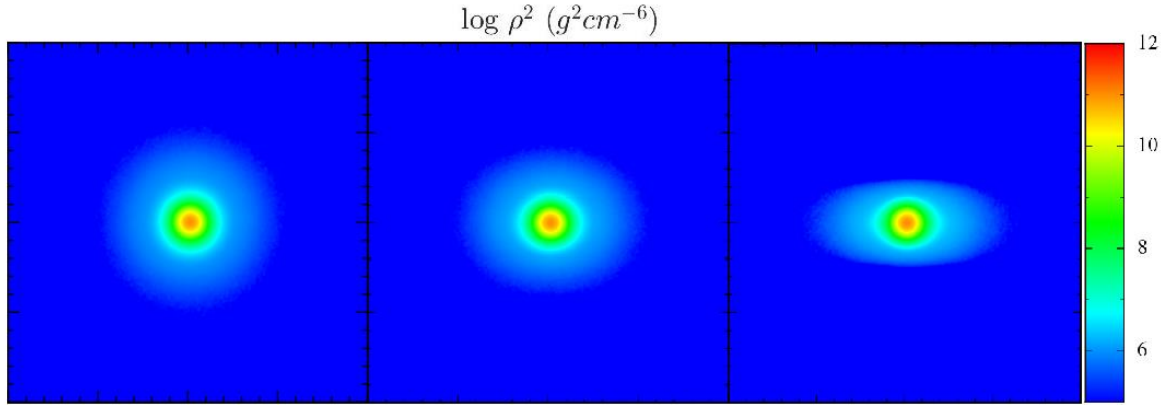


**Figure 13.** Logarithm of the square density of the remnant of the simulation 0.3+0.6 (HR) solar masses for three angles of sight: 0 degrees on the left panel, 45 degrees on the center panel and 90 degrees for the right panel. The distance tick unit is 0.02 solar radii.

computed using the real gravitational potential, not the point-mass approximation.

Moreover, comparing with previous works [Lorén-Aguilar et al. 2009; Aznar-Siguán et al. 2014], there is not a plateau at small times. The reason for this is the distribution of eccentricities of the accreted particles, since in this work we find smaller eccentricities.

As it should be expected, the more violent interaction is, the higher the fallback luminosity is. The more massive mergers produce more material in the disk with larger kinetic energies, thus resulting in enhanced fallback luminosities.

#### 4.6.4. Optical appearance

Finally, the optical appearance of the remnant of the 0.3+0.6 (HR) simulation is discussed below. The logarithm of the square density is rendered in Fig. 13 at the end of the simulation. The plots are taken for different angles of sight with respect to the equatorial plane (0, 45 and 90 degrees from left to right). As it can be seen, the remnant is a compact spherical object surrounded by an accretion disk and a debris region. As previously said, the density reaches the minimum value that code can achieve (light blue color).

# 5. SUMMARY AND CONCLUSIONS

Five simulations of the merger between two white dwarfs were made with a smoothed particle hydrodynamics numerical code. We used 200,000 SPH particles per star in four of them, and an increased resolution of 500,000 particles for the secondary star in one case. In all cases, the secondary white dwarf (the less massive one) was made of helium, while the primary (the more massive star) was made of carbon and oxygen. In all cases, the total mass of the system was less than the Chandrasekhar mass limit. One of the main objectives of the study was to analyze whether sub-Chandrasekhar systems may potentially achieve the conditions to produce a Type Ia event. Studying the results of each simulation, we find that given the temperatures achieved during the merging process, it is clear that some cases could potentially lead to such an event. However, this conclusion has to be taken with some caution, because although the potential initial conditions to trigger a carbon detonation are reached, the result of such an ignition could not be necessarily a supernova explosion. Carbon ignition is a just necessary condition for the occurrence of a supernova. Following the process up to the explosive stage is an extremely complex task, which is well beyond the scope of this work.

We have shown how the final configuration of the remnant consists of a central compact object, which rotates as a rigid body, surrounded by a hot rapidly rotating corona, a Keplerian disk around it and a debris region. We also showed how the secondary white dwarf is disrupted during the merging process, forming a tidal stream. When the tidal stream is formed, it expands and cools. As time passes by, the velocity of the stream of particles becomes tangent to it, stopping its expansion. After some time the tidal stream is fragmented in small clumps. This fragmentation occurs progressively, starting in the tail of the stream and propagating through it. After analyzing the velocity profile of the particle field we discarded the presence of any self-gravitating fragmentation, since the particles strictly followed the stream without showing any evidence of local collapse. We also discarded any compositional effect, since the density of the stream is uniform. As previously mentioned, the code has a minimum density threshold in density, in order to prevent numerical noise in the scattered particles around the merger. Hence, the changes in density, sound speed and temperature for the tidal stream particles are extremely small. As a consequence, there seem to be no pressure in-homogeneities capable of explaining the clumps. Hence, we concluded that possibly the cause of the clump formation was an uneven distribution of particles caused by a limited numerical resolution, probably enhanced by the stickiness caused by the excess of numerical viscosity inherent to the SPH method. A thorough study of this possibility, unfortunately, has been left for future studies due to the lack of time. To properly resolve the inner structure of the clumps, we should increase the space resolution

of the simulations by at least an order of magnitude. But this would require an increase of the number of particles by more than two orders of magnitude. The time needed to run simulations with such a number of particles was way longer than the duration of the project, so it will be left for a future study.

It is also worth mentioning that even if a SN Ia event does not occur, the remnant of a merger of white dwarfs can still lead to very interesting objects. For example, the chemical composition of the disk formed during the merger simulation composed of 0.3+1.0 solar masses shows enrichment in heavy elements like Ne, Mg, Si and S, due to the nuclear reactions occurring during the merger. Such burning substantially increases the metallicity of the accretion disk, producing a natural environment where planets and asteroids may be formed. This could explain a fraction of the metallic abundances found in some hydrogen-rich white dwarfs which are surrounded by dusty disks [Jura [2003](#)].

Moreover, the gravitational waves of each simulation were computed and shown to be strong enough to be detectable by eLISA, with the only exception of the 0.2+0.6 solar masses run, whose orbital frequency turns out to be too small to be detected. We have proved as well the existence of a direct correlation between the maximum temperature achieved during the merging phase, and the thermal neutrino emission rate. Finally, regarding the high-energy photons produced in the aftermath of the merger, the more violent interaction is, the higher the fallback luminosity is.

## 6. REFERENCES

### A

Aznar-Siguán G., García-Berro E., Lorén-Aguilar P., José J., Isern J., 2013, MNRAS, 434, 2539.

Aznar-Siguán G., García-Berro E., Lorén-Aguilar P., 2014, MNRAS, 443, 2372.

Aznar-Siguán G., García-Berro E., Lorén-Aguilar P., Soker N., Kashi A., 2015, MNRAS, 450, 2948.

### B

Balsara D. S. 1995, J. Comp. Phys., 121, 357.

Barnes J., Hut P., 1986, Nature, 324, 446.

Benz W., Cameron A. G. W., Bowers R. L., 1989a, in White Dwarfs, Proc. of the ed. Wegner G., LNP 328 (Berlin: Springer-Verlag) IAU Coll., 114, 511.

Benz W., Thielemann F. K., Hills J. G., 1989b, ApJ, 342, 986.

Benz W. Cameron A. G., Press W. H., Bowers R.L. 1990, A&A, 348, 647.

Bildsten L., Shen K. J., Weinberg N. N., Nelemans G., 2007, ApJ, 662, L95.

### C

Chiosi E., Chiosi C., Trevisan P., Piovan L., Orio M., 2015, MNRAS, 448, 2100.

Clement M. J., 1974, ApJ, 194, 709.

### G

Giacomazzo B., Rezzolla L., Baiotti L., 2011, Phys. Rev. D, 83, 044014.

Gingold R. A., Monaghan J. J., 1977, MNRAS, 181, 375.

Guerrero J., García-Berro E., Isern J., 2004, A&A, 413, 257.

## **H**

Han Z., Podsiadlowski P., 2004, MNRAS, 350, 1301.

Hillebrandt W., Kromer M., Röpke F. K., Ruitter A. J., 2013, Frontiers Phys., 8, 116.

## **I**

Iben I. J., Tutukov A., V., 1984, ApJS, 54, 335.

Ilkov M., Soker N., 2012, MNRAS, 419, 1695.

Ilkov M., Soker N., 2013, MNRAS, 428, 579.

Itoh N., Totsuji H., Ichimaru S., Dewitt H. E., 1979, ApJ, 234, 1079.

Itoh N., Hayashi H., Nishikawa A., Kohyama Y., 1996, ApJS, 102, 411.

## **J**

Jura M., 2003, ApJ, 584, L91.

## **K**

Kashi A., Soker N., 2011, MNRAS, 417, 1466.

Kunugise T., Iwamoto K., 2007, PASJ, 59, L57.

Kushnir D., Kats B., Dong S., Livne E., Fernández R., 2013, ApJ, 778, L37.

## **L**

Livio M., Riess A. G., 2003, ApJ, 594, L93.

Livne E., Arnett D., 1995, ApJ, 452, 62.

Lorén-Aguilar P., Guerrero J., Isern J., Lobo J. A., García-Berro E., 2005, MNRAS, 356, 627.

Lorén-Aguilar P., Isern J., García-Berro E., 2009, A&A, 500, 1193.  
Lorén-Aguilar P., Isern J., García-Berro E., 2010, MNRAS, 406, 2749.  
Lucy L. B., 1977, AJ, 82, 1013.

## **M**

Misner C. W., Thorne K. S., Wheeler J. A., 1973, Gravitation W. H. Freeman and Co.  
Mochkovitch R., Livio M., 1989, A&A, 209, 111.  
Mochkovitch R., Livio M., 1990, A&A, 236, 378.  
Monaghan J. J., Gingold R. A. 1983, J. Comp. Phys. 52. 374  
Monaghan J. J., Lattanzio J. C., 1985, A&A, 149, 135.  
Monaghan J. J., 1997, J. Comp. Phys., 136, 298.

## **N**

Nomoto K., 1982, ApJ, 257, 780.

## **O**

Odrzywolek A., Plewa T., 2011, A&A, 529, A156.

## **P**

Papish O., Soker N., García-Berro E., Aznar-Siguán G., 2015, MNRAS, 449, 942.

## **R**

Rasio F. A., Shapiro S. L., 1995, ApJ, 438, 887.  
Raskin C., Timmes F. X., Scannapieco E., Diehl S., Fryer C., 2009, ApJ, 399, L156.

Rauscher T., Thielemann F. K., 2000, *Atom. and Nucl. Data Tabl.*, 75, 1.

Ritossa C., García-Berro E., Iben I., 1996, *ApJ*, 469, 489.

Rosswog S., 2007, *MNRAS*, 376, L48.

Rosswog S., Kase, D., Guillochon J., Ramirez-Ruiz E., 2009, *ApJ*, 705, L128.

Ruiz-Lapuente P., 2014, *New Astron. Rev.*, 62, 15.

## S

Segretain L., Chabrier G., Hernanz M., García-Berro E., Isern J., 1994, *ApJ*, 434, 641.

Segretain L., Chabrier G., Mochkovitch R., 1997, *ApJ*, 481, 355.

Serna A., Alimi J. M., Chieze J. P., 1996, *ApJ*, 461, 884.

Shen K. J., Bildsten L., 2009, *ApJ*, 699, 1365.

Shen K. J., Guillochon J., Foley R. J., 2013, *ApJ*, 770, L35.

Shen K. J., Bildsten L., 2014, *ApJ*, 785, 61.

Soker N., 2011, *Proc. Int. Astron. Union*, 7, 72.

Soker N., Kashi A., García-Berro E., Torres S., Camacho J., 2013, *MNRAS*, 431, 1541.

## T

Thompson T. A., 2011, *ApJ*, 741, 82.

Tornambé A., Piersanti L., 2013, *MNRAS*, 431, 1812.

Tsebrenko D., Soker N., 2015, *MNRAS*, 447, 2568.

## V

van Kerkwijk M. H., Chang P., Justham S., 2010, *ApJ*, 722, L157.

## W

Webbink R. F., 1984, ApJ, 277, 355.

Whelan J., Iben Jr. I., 1973, ApJ, 186, 1007.

Woosley S. E., Weaver T. A., 1994, ApJ, 423, 371.

## Y

Yoon S. C., Podsiadlowski P., Rosswog S., 2007, MNRAS, 380, 933.